Received: 8 October 2022 | Accepted: 13 October 2022

DOI: 10.1002/pamm.202200238

Analysis of a phase-field finite element implementation for precipitation

Ali Reza Safi[1], **Rupesh Chafle**[1,*], and **Benjamin Klusemann**[1,2]

[1] Solid State Materials Processing, Institute of Materials Mechanics, Helmholtz-Zentrum Hereon, Max-Planck-Straße 1, 21502 Geesthacht, Germany

[2] Institute of Product and Process Innovation, Leuphana Universtiy Lüneburg, Universitätsallee 1, 21335 Lüneburg, Germany

Precipitation hardening is an essential mechanism in materials design of age-hardenable aluminium alloys. The occurrence and distribution of nano-sized particles in such alloys can lead to superior material properties. During thermo-mechanical processing, these particles evolve dynamically as function of temperature and applied load. Therefore, sophisticated modelling frameworks are required to study the underlying phenomena of this microstructural evolution in depth. Phase-field method based on the diffuse interface approach has been successfully employed in literature to study particle nucleation and growth, as well as equilibrium particle shapes. Although phase-field models provide reliable results due to the flexible adaption of the free energy, the method is computationally expensive, requiring efficient solution schemes. The finite-element discretization in deal.II can overcome scalability disadvantages and can outperform standard finite-difference codes. In this work, we used adaptive mesh refinement and adaptive time-stepping and investigate how AMR and the use of the same stiffness matrix for a certain amount of time steps affect the performance of the phase-field model. Particle growth simulations are performed to outline the major benefits of the finite element phase-field model. The numerical strategy is shown to be effective regardless of the initial particle shape by considering different particle morphologies. The results illustrate a significant increase in simulation performance with the applied numerical techniques.

1 Introduction

The microstructure of a heterogeneous material can be described via the spatial distribution of features such as crystal orientation, phases, structural variants and concentration of alloying elements. Material properties are determined by the size, shape, volume fraction, and spatial arrangement of such microstructural features. During processing, the specific material as well as the process parameters influence the microstructure, which can significantly affect the product properties. In age-hardenable aluminium alloys, such as Al-Cu-Li alloys, the formation and evolution of precipitates during heat treatment or thermo-mechanical processing is considered one of the main strengthening mechanisms [1]. Precipitates form a barrier for dislocations which can either cross the particle through shearing or Orowan looping [2]. This leads to an increase in the required stress for a particular slip system to enable dislocation motion, causing an increase in the macroscopic yield strength of the material. Understanding the formation and evolution mechanisms is a crucial step in alloy and process design. Experimental characterization of precipitates requires the application of costly methods such as scanning electron microscopy (SEM) or transmission electron microscopy (TEM) for ex-situ measurements or synchrotron measurements for in-situ applications [3]. Performing measurements for a broad spectrum of chemical alloy compositions and various process conditions becomes unwieldy. Alternatively, using mathematical models to study particle evolution is an attractive option that yields statistically meaningful data and allows for efficient three-dimensional (3D) simulations.

Developing a modelling framework that respects the underlying mechanisms is necessary to study particle growth in supersaturated domains. Among the wide range of applicable models, such as the Kolmogorov-Johnson-Mehl-Avrami [4] or Kampmann-Wagner models [5], the phase-field (PF) method is a well-established and reliable framework. Using the PF method, it is possible to study the time-dependent variation of conserved and non-conserved quantities, such as solute concentration, structural variants, grain orientation etc. Across the interface regime, the PF variable changes smoothly, which allows for a robust mathematical treatment. Thus, the interface is treated as a so-called diffuse interface which, unlike sharp interface approaches, does not require explicit interface tracking. Additionally, the PF method allows for coupling with the CALculation of PHAse Diagrams (CALPHAD) framework [6], making it possible to establish meaningful linkages between process parameters, chemical composition and (micro-)structure [7].

In this work, we employ a finite-element implementation of the PF model (FE-PFM), allowing for the adoption of adaptive time stepping, adaptive mesh refinement (AMR) and the use of the same stiffness matrix for a defined amount of time steps. We aim to enhance the model's performance and demonstrate the improvement with the help of several test cases.

* Corresponding author e-mail: rupesh.chafle@hereon.de

2 Phase-field model

In this work, we consider a binary system whose total free energy consists of contributions from the bulk and interface as expressed by

$$F_{total} = \int_V \left[f(c) + \frac{1}{2}\kappa \left[\nabla c\right]^2 \right] dV, \tag{1}$$

where c is the concentration of the solute element, $f(c)$ is the bulk free energy density, and V is the volume of interest [8]. Here, we assume isotropic interfacial energy by considering a constant gradient energy coefficient κ. $f(c)$ can be expressed as a double-well potential in the following manner

$$\mathrm{f}\left(c\right) = A\, c^2 \left[1-c\right]^2, \tag{2}$$

with A being a positive constant which determines the height of the energy barrier between the two phases. Since concentration is a conserved variable, its temporal evolution is described using the 4th-order partial differential Cahn-Hilliard equation [8]

$$\frac{\partial c}{\partial t} = M\, \nabla^2 \left(\frac{\partial F_{total}}{\partial c} \right), \tag{3}$$

where M is the mobility/diffusion coefficient. Here, we consider an isothermal problem and neglect the composition dependency of M, which makes it constant in V. The spatio-temporal evolution of c is driven by the minimization of F_{total}.

3 Numerical implementation

In this work, we approach Eq. (3) using a finite-element (FE) solution scheme. The presence of 4th-order spatial derivatives in the Cahn-Hilliard equation does not allow for the use of linear shape functions with C^0 continuity. Alternatively, it is possible to use higher-order Hermite shape functions with C^1 continuity, however, which increases the computational costs significantly [9]. Following Elliott et al. [10], to overcome this problem, Eq. (3) is reformulated into two coupled equations, introducing a new variable μ as follows

$$\frac{\partial c}{\partial t} - M\, \nabla^2 \mu = 0, \tag{4}$$

$$\mu - \frac{\partial f}{\partial c} + \frac{1}{2}\kappa \left(\nabla c\right)^2 = 0. \tag{5}$$

Eqs. (4) and (5) only contain 2nd-order spatial derivatives, which permits the use of linear shape functions. Conveniently, μ has a thermodynamic meaning and is known as the chemical potential. These are cast into weak forms by multiplying them with the test functions η and ζ, respectively, and integration over the domain of interest leads to

$$\int_V \frac{\partial c}{\partial t}\, \eta \, dV + \int_V M\, \nabla \mu \cdot \nabla \eta \, dV = 0, \tag{6}$$

$$\int_V \mu\, \zeta \, dV - \int_V \frac{\partial f}{\partial c}\, \zeta \, dV - \int_V \kappa\, \nabla\, c \cdot \nabla \zeta \, dV = 0. \tag{7}$$

The time discretization of Eqs. (6) and (7) is performed via an implicit Euler scheme. The residual local element vector components R^e_c and R^e_μ in their time-discretized forms are formulated in the following manner

$$R^e_c = \int_V \left[\left(c^{n+1} - c^n\right)\, \eta + dt\, M \nabla \mu^{n+1}\, \cdot \nabla \eta \right] \, dV, \tag{8}$$

$$R^e_\mu = \int_V \left[\mu^{n+1}\, \zeta - \frac{\partial f^{n+1}}{\partial c}\, \zeta - \kappa\, \nabla c^{n+1}\, \cdot \nabla \zeta \right] \, dV. \tag{9}$$

The components K^e_{cc}, $K^e_{c\mu}$, $K^e_{\mu c}$ and $K^e_{\mu\mu}$ of the local element stiffness matrix $\mathbf{K}^e$ are defined as the derivative of the local element residual vector components with respect to ∂c and $\partial \mu$, leading to

$$\mathbf{K}^e = \begin{bmatrix} K^e_{cc} & K^e_{c\mu} \\ K^e_{\mu c} & K^e_{\mu\mu} \end{bmatrix} = \begin{bmatrix} \frac{\partial R^e_c}{\partial c} & \frac{\partial R^e_c}{\partial \mu} \\ \frac{\partial R^e_\mu}{\partial c} & \frac{\partial R^e_\mu}{\partial \mu} \end{bmatrix}. \tag{10}$$

By calculating the local residual vector components R_c^e and R_μ^e, and the local stiffness matrix $\mathbf{K}^e$, the global residual vector components R_c^G and R_μ^G and the global stiffness matrix $\mathbf{K}^G$ can be assembled as their sum, respectively. The resulting nonlinear equation system becomes

$$\begin{bmatrix} K_{cc}^G & K_{c\mu}^G \\ K_{\mu c}^G & K_{\mu\mu}^G \end{bmatrix} \begin{bmatrix} \Delta c \\ \Delta \mu \end{bmatrix} = \begin{bmatrix} R_c^G \\ R_\mu^G \end{bmatrix}. \tag{11}$$

The implicit system of equations is solved using the Newton-Raphson method summarized in Alg. (1). Here, we select exemplary values for M, κ, and the initial time step dt_0 with adaptive time-stepping employed and periodic boundary conditions being applied. n_s and n_K are the current time step counter and the required steps to perform stiffness matrix assembly, respectively. The model is implemented in the deal.II library, which uses Open MPI for parallelization and the P4est library for AMR [11].

Algorithm 1: Modified Newton-Raphson algorithm for the solution of the implicit Cahn-Hilliard equation

Data: $c(t=0s); \mu(t=0s)=0$ at V
Result: $c(t); \mu(t)$at V
$M \leftarrow 1.0$;
$\kappa \leftarrow 0.5$;
$dt_0 \leftarrow 0.02$;
$n_s \leftarrow 0$;
while $t < t_{max}$ **do**
  $n_s \leftarrow n_s + 1$;
  if $n_s = n_K$ **then**
    $n_s \leftarrow 0$;
    while $e < n_{elements}$ **do**
      while $q < n_{quadrature\ points}$ **do**
        Calculate $\frac{\partial^2 f}{\partial c^2}$
        Calculate contribution to $\mathbf{K}^e$
      end
      $\mathbf{K}^G \leftarrow \mathbf{K}^G + \mathbf{K}^e$;
    end
  end
  while $iter < iter_{max}$ & $[|R_c^G| + |R_\mu^G|] > tol$ **do**
    while $e < n_{elements}$ **do**
      while $q < n_{quadrature\ points}$ **do**
        Calculate $\frac{\partial f}{\partial c}$
        Calculate contribution to R_c^e and R_μ^e
      end
      $R_c^G \leftarrow R_c^G + R_c^e$;
      $R_\mu^G \leftarrow R_\mu^G + R_\mu^e$;
    end
    Solve Eq. (11)
    Update c and μ
    if $iter > 0.8 iter_{max}$ **then**
      $dt \leftarrow 0.5 dt$;
    end
    if $iter < 0.3 iter_{max}$ **then**
      $dt \leftarrow 2.0 dt$;
    end
  end
end

4 Results

This section presents the results of our studies conducted with the FE-PFM. First, a circular particle-matrix problem is investigated to evaluate the effect of the AMR algorithm on performance increase. We then highlight the advantages of using the modified Newton-Raphson (MNR) solution scheme. Lastly, different particle morphologies have been investigated for their effects on simulation time.

4.1 Adaptive mesh refinement

This section focuses on establishing the effect of AMR on the simulation performance. When performing simulations using a regular mesh, the complete domain is meshed according to the required mesh size at the diffuse interface to ensure convergence. Consequently, regular meshes can lead to element sizes which are smaller than necessary in the matrix area and the particle bulk. To overcome this limitation, AMR can be employed. It is a method which can resolve areas of interest and decrease the mesh size in other parts of the domain. Within deal.II, the mesh is described using an octree data structure. The mesh is generated by initiating a single square element and successively refining it to smaller ones. During AMR, the algorithm coarsens or refines elements according to the defined AMR condition, here the concentration gradient. AMR produces nodes which may be members of a particular element but do not belong to the neighboring element due to the different refinement levels present. These nodes are referred to as hanging nodes and require special treatment as they result in discontinuous shape functions. The deal.II library provides the functionalities to handle hanging nodes effectively. To perform AMR, a condition which classifies elements for refining or coarsening must be defined.

A 40×40 simulation domain with a circular particle of diameter 10 serves as an initial condition. The particle is initialized with a solute concentration of 1.0 and the matrix contains a total supersaturation of 10 %, i.e. 0.1 solute concentration. This ensures that the particle will not shrink due to the Gibbs-Thomson effect [12]. The global refinement level n_r defines the number of elements, i.e. 4^{n_r} in 2D. The initial global refinement levels are selected as 7, 8 and 9, which correspond in 2D to an effective element number of 16384, 65536 and 262144, respectively. Elements are allowed to refine or coarsen a maximum of 2 levels with respect to their initial global refinement level.

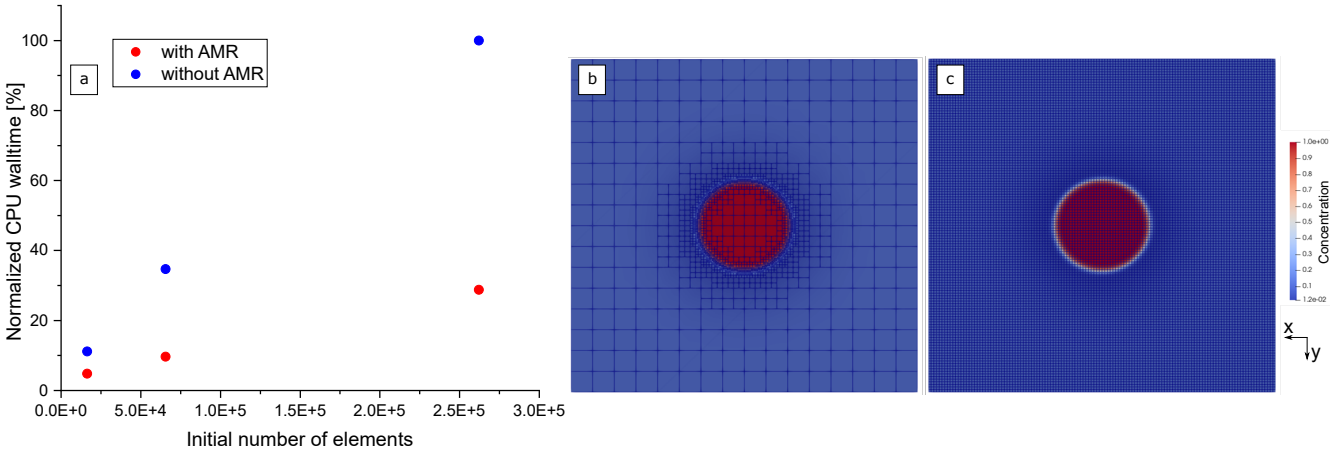

Fig. 1: (a) Normalized required CPU walltime to reach 30 s simulation time for different initial refinement levels. Concentration maps (b) with and (c) without AMR for an initial refinement level of 7.

Figure 1 shows the result of the particle simulation at a simulated time of 30 s. A normalized walltime is shown in Fig. 1(a) based on the largest initial mesh without AMR. It is shown that the simulations with AMR require much less computation time, where the effect of AMR increases with an increased level of initial global refinement. Two simulation results for a refinement level of 7 with and without AMR are illustrated in Fig. 1. The algorithm successfully coarsens bulk areas of nearly constant concentration while refining the diffuse interface due to the high concentration gradients. Although the interface is refined to a level of 9 in Fig. 1(b), this setup contains significantly fewer elements than the analogous case without AMR shown in Fig. 1(c).

4.2 Modified Newton-Raphson solution scheme

Based on Alg. 1 of the implicit FE-PFM, the (chemical) stiffness matrix is assembled at the beginning of each time step and afterwards inverted, representing one of the most time-intensive steps in the model during the calculation. To reduce the computational effort, this approach can be modified by using the identical stiffness matrix for a certain amount of time steps, leading to a MNR solution scheme. To investigate the effect and the error contribution of the MNR approach, simulations are performed on 5 different particle morphologies: trigon, tetragon, pentagon, hexagon and circle. Each morphology has the same size, with an area of 173.205, and the minimal possible interface, i.e. the trigon is represented by an equilateral triangle, the tetragon by a square, etc. The domain size is 40×40, the particles are initialized with a solute concentration of 1.0, and the matrix contains a total supersaturation of 10 % , i.e. 0.1 concentration. Each case is simulated using six different steps to recalculate the stiffness matrix, i.e. after 1, 2, 4, 8, 16, and 32 time steps.

Figure 2(a) shows the efficiency of the simulations evaluated at a total simulated time of 80 s. The CPU walltimes for each particle case are normalized with respect to their corresponding reference case. It can be seen that regardless of the particle shape, a reduced number of re-evaluation steps for the stiffness matrix and its inverse leads to an increase in computational efficiency. While the trigon and the tetragon benefit from a reduced walltime of about 12 %, the other shapes experience an

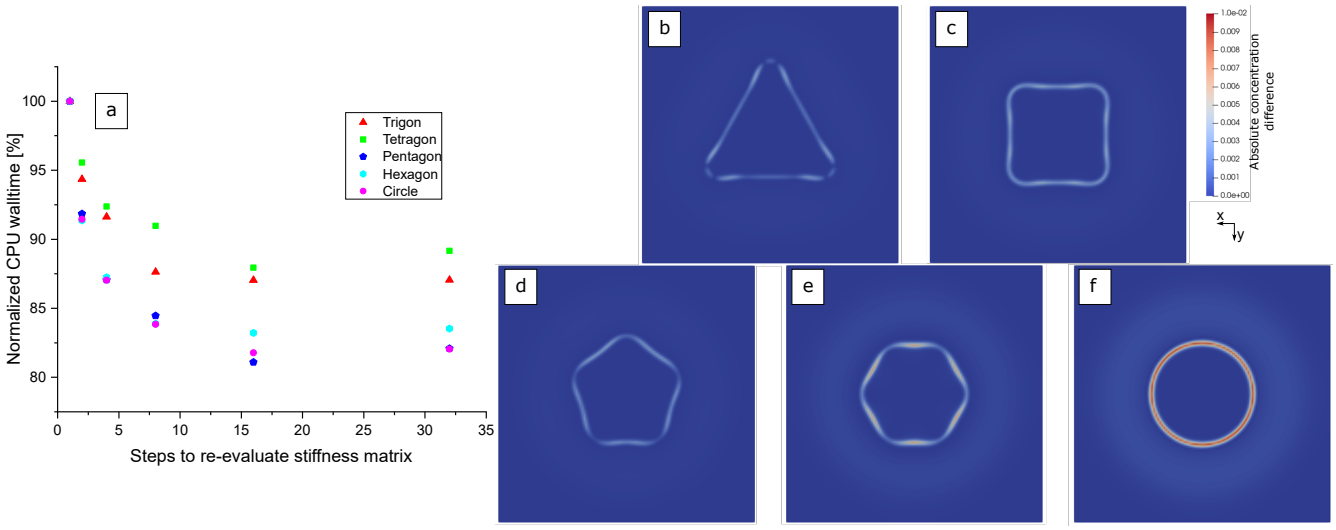

Fig. 2: (a) Normalized CPU walltime to reach 80 s simulation time for steps to recalculate the stiffness matrix. (b-f) Resulting absolute concentration difference between the reference case, i.e. re-evaluating the stiffness matrix after each step, and the lowest frequent assembly for all particle shapes.

increased efficiency of more than 15 % if only after 16 time steps the stiffness matrix is re-evaluated. An additional increase in gaps between re-evaluation does not increase the efficiency further as the resulting equation system requires more iteration steps for the Newton-Raphson scheme and, hence, causes a decreased time step due to adaptive time stepping. In Fig. 2(b-f) the resulting error is illustrated. As expected, the error at the interface is the highest due to the dynamic behaviour in this regime. However, the error is in a reasonable range with respect to increased efficiency.

4.3 Influence of particle morphology

Although the improved efficiency of the modified scheme could be shown regardless of the particle shape, differences between particle shapes are notable. To evaluate the sole effect of particle morphology on the computational effort, the computational times of each reference case demonstrated in section 4.2 are compared to each other with respect to the circumference-to-area ratios of the particles.

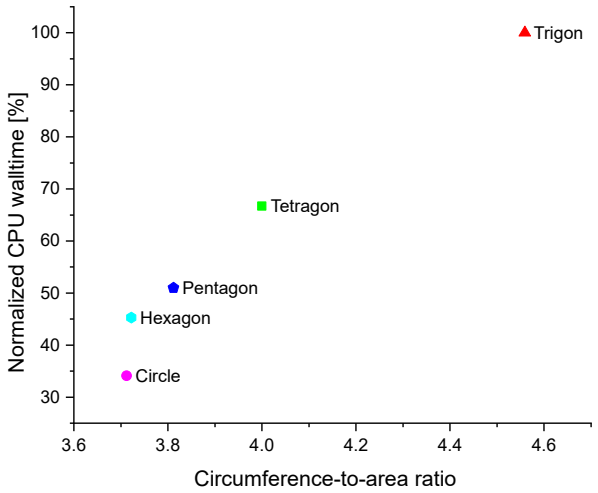

Fig. 3: Influence of different particle morphologies, quantitatively described using the circumference-to-area ratio, on the required computation time, normalized with respect to the computation time of the trigon.

Figure 3 illustrates the effect of the particle shape on the computation time. It can be seen that particles which have a small interface with respect to their area require less computation time than particles with a large interface. For instance, the simulation with the circular particle requires 65 % less computation time compared to the trigon. Since the interface is in a non-equilibrium state, Eq. (2), the interface elements are numerically mainly responsible for the increase in computation time.

5 Conclusion

This work demonstrates different aspects influencing the numerical efficiency of a PF implementation on the basis of finite elements. Applying AMR is especially suitable for studies where the subject of interest lies in a comparably small regime in the domain, such as the presented particle growth simulations. The refinement of the interface and the coarsening of bulk areas lead to a significant increase in computational efficiency. The application of a MNR scheme, i.e. a reduced number of re-evaluation steps of the (chemical) stiffness matrix, leads to a considerable increase in performance without significant compromise in accuracy for the currently investigated particle shapes. Finally, we establish the influence of particle morphology on computation time. The circumference-to-area ratio is identified as a major contribution in terms of simulation speed, as it indicates the amount of interface element present in the domain, which causes an increase in computational costs.

Acknowledgements This project has received funding from the European Research Council (ERC) under the European Union's Horizon 2020 research and innovation programme (grant agreement No 101001567). Open access funding enabled and organized by Projekt DEAL.

References

[1] T. Gladman, Mater. Sci. Technol. **15**, pp. 30–36 (1999).
[2] E. Orowan, Z. Physik **89**, pp. 634–659 (1934).
[3] J. F. dos Santos, P. Staron, T. Fischer, J. D. Robson, A. Kostka, P. Colegrove, H. Wang, J. Hilgert, L. Bergmann, L. L. Hütsch, N. Huber and A. Schreyer, Acta Mater. **148**, pp. 163–172 (2018).
[4] J. D. Robson and H. K. D. H. Bhadeshia, Mater. Sci. Technol. **13**, pp. 631–639 (1997).
[5] J. Herrnring, B. Sundman, P. Staron and B. Klusemann, Acta Mater. **215**, pp. 117053 (2021).
[6] A. K. Mallik, Bull. Mater. Sci. **28**, pp. 107–121 (1986).
[7] C. Liu, A. Davis, J. Fellowes, P. B. Prangnell, D. Raabe and P. Shanthraj, Acta Mater. **226**, pp. 117602 (2022).
[8] J. W. Cahn and J. E. Hilliard, J. Chem. Phys. **28**, pp. 258–267 (1958).
[9] L. Zhang, M. R. Tonks, D. Gaston, J. W. Peterson, D. Andrs, P. C. Millett and B. S. Biner, J. Comput. Phys. **236**, pp. 74–80 (2013).
[10] C. M. Elliott, D. A. French and F. A. Milner, Numer. Math. **54**, pp. 575–590 (1989).
[11] D. Arndt, W. Bangerth, B. Blais, M. Fehling, R. Gassmöller, T. Heister, L. Heltai, U. Köcher, M. Kronbichler, M. Maier, P. Munch, J. P. Pelteret, S. Proell, K. Simon, B. Turcksin, D. Wells and J. Zhang, J. Numer. Math. **29**, pp. 171–186 (2021).
[12] W. C. Johnson and P. W. Voorhees, Metall. Mater. Trans. A **18**, pp. 1213–1228 (1987).